OPEN ACCESS

University of BRISTOL

Peer reviewed version

Link to published version (if available):
10.1016/j.jnucmat.2018.08.033

Link to publication record in Explore Bristol Research

PDF-document

University of Bristol - Explore Bristol Research
General rights

UNDERSTANDING IRRADIATION-INDUCED NANOPRECIPITATION IN ZIRCONIUM ALLOYS USING CORRELATIVE TEM AND APT

A. Harte[1], R. Prasath Babu[1], C. Hirst[2], T. Martin[2], M. Moody[2], P. Frankel[1], J. Romero[3], L. Hallstadius[4], E. C. Darby[5], M.Preuss[1]

[1]The University of Manchester, Manchester Materials Science Centre, Grosvenor Street, Manchester, M13 9PL, United Kingdom

[2]The University of Oxford, United Kingdom

[3]Westinghouse Electric Company, Columbia, SC, United States

[4]Westinghouse Electric Sweden AB, SE---72163 Västerås, Sweden

[5]Rolls Royce Plc., Nuclear Materials, Derby, UK

Contact: Allan Harte, allan.harte@manchester.ac.uk

1   ABSTRACT

We characterise irradiation-induced precipitation at the nano-scale in a Zr-Sn-Fe-Cr-Ni-alloy (Zircaloy-2) combining for the first time scanning transmission electron microscopy (STEM) with high resolution energy dispersive X-ray (EDX) spectroscopy and complimentary atom probe tomography (APT) and diffraction TEM techniques. We find that Fe- and Cr-rich nano-rods precipitate in Zircaloy-2 following proton irradiation at 350 °C to low dose ~2 dpa. The nano-rods are long in a direction 12-15° from the Zr matrix $\langle 0001 \rangle$, align in the basal plane and are of length 5-30 nm and of width 1.5-5 nm. Smaller rods are of APT-determined composition $Zr_4(Fe_{0.67}Cr_{0.33})$, tending towards $Zr_3(Fe_{0.69}Cr_{0.31})$ as the rod volume increases to $> ~400$ nm^3, in agreement with STEM-EDX determination of composition resembling that of Zr_3Fe with Cr replacing some of the Fe. The Fe/Cr ratio has been shown to increase with distance

from the nearest partially-dissolved Zr(Fe,Cr)$_2$ SPP. The implications for macroscopic irradiation-induced growth, irradiation-induced hardening and the interaction of clusters with dislocation loops are discussed.

2   INTRODUCTION

Zr alloys are used as the cladding and structural components of nuclear reactor cores due to their low average neutron absorption cross section and their retention of mechanical properties and corrosion resistance at operating temperatures [1]. Of the common alloying elements of Zr in the Zircaloy family of alloys, Fe, Cr and Ni, the light transition elements, are of low solubility in the α-Zr matrix [2–4] and precipitate as thermodynamically stable second phase particles (SPPs) in both the matrix and at grain boundaries [5–8]. The Sn remains homogenous in solid solution at low concentrations and acts as an α-stabiliser such that supersaturated solid solutions of Zr-6.5Sn (at.%) are stable up to 953 °C as α-phase [9]. Alloy corrosion behaviour and the resulting hydrogen ingress depends on the type and morphology of SPPs [10,11]. Better corrosion resistance has been correlated to reduced irradiation-induced growth strain [11] and SPPs and other chemical effects are known to play a role in the type, density and spatial relationship of dislocations that form as a result of irradiation [12–15].

SPPs in the Zircaloys are known to undergo irradiation-induced dissolution processes at intermediate to high neutron irradiation temperatures (280-450 °C), depleting preferentially in Fe but also in Cr and Ni in the Zr(Fe,Cr)$_2$ and Zr$_2$(Fe,Ni) SPPs, respectively [6,16–23,11]. It is therefore important to study the results of this dissolution and what it means for the microstructure-related performance properties.

During irradiation the Zr matrix becomes increasingly saturated in solute elements and has been shown to precipitate new rod-shaped Fe-, Cr- and Ni- rich phases, extending throughout the matrix with a rod-like morphology [17,24] and in higher concentration close to partially dissolved SPPs [25] compared to other parts of matrix. Binary Zr-Fe phases, most notably Zr_3Fe, have been reported to nucleate during irradiation under PWR conditions in Zircaloy-4 [26] and under BWR conditions in Zircaloy-2 [27]. Such phases are thought to be relatively resistant to neutron irradiation at ~315-350 °C [26,28]. More recently, smaller clusters have been observed in high number density in Zircaloy-2, neutron-irradiated in a BWR to high fluences of 16.5 $\times 10^{25}$ n m^{-2} ~27.5 dpa [29], and the growth of small Fe, Cr clusters has been suggested as dependent on the presence of Zr vacancies [30]. These small clusters or rods are likely to have significant effect on not only the ongoing radiation damage accumulation but also on mechanical properties such as irradiation-induced hardening [31,32].

As an analogue to neutron irradiation, we aim to assess the irradiation-induced precipitation in Zircaloy-2 after exposure to low dose proton irradiation. We observe nanoprecipitation in the matrix and use high resolution correlative techniques for their characterisation. For the first time we use both atom probe tomography and scanning transmission electron microscopy with significant energy-dispersive X-ray spectroscopy capability to investigate both the compositional and crystallographic properties of the precipitates.

3 EXPERIMENTAL

3.1 MATERIAL

Fully recrystallised Zircaloy-2 plate was provided by Westinghouse Electric Company with nominal composition Zr-1.5Sn-1.4Fe-0.1Cr-0.06Ni (wt.%) [1], an equiaxed grain size in the range ~5-15 μm diameter and a strong basal texture in the normal direction, split ± 30° in the transverse direction. The plate was cut into bars of dimensions 2 x 2 x 20 mm and mechanically polished from the normal direction to a quality suitable for electron backscatter diffraction, such that the grains were visible by polarised light microscopy. The bars were then proton-irradiated in the normal direction at the Michigan Ion Beam Laboratory's 1.7 MeV Tandertron accelerator facility at 2 MeV and 350 ±9 °C and a current of ~0.2 μA mm^{-2} for a total of 96 hr. The proton irradiation dose in displacements per atom (dpa) was calculated by the quick Kinchin-Pease calculation in SRIM as recommended by Stoller *et al.* [33] in pure, amorphous Zr with a displacement energy (E_d) of 40 eV [34]. The calculated dose level as a function of proton penetration depth is shown in Figure 1, in which three depths are highlighted; 0.5 μm at which depth the atom probe tomography (APT) needles were extracted, 12 μm at which depth the electropolished foils were prepared for transmission electron microscopy (TEM) analysis, and 29 μm, the Bragg peak. As such, the APT data is obtained from material after ~1.5 dpa at a damage rate ~4.3 x10^{-6} dpa s^{-1} and the TEM analysis after ~2.3 dpa and ~6.7 x10^{-6} dpa s^{-1}.

3.2 ANALYSIS

For APT analysis, both irradiated and non-irradiated samples were mounted on arrays

of silicon micro tips and annular milled with a gallium focused ion beam to obtain sharp needles with an end radius of ~50nm. This was accomplished by milling with successively smaller annular masks and successively lower gallium ion currents on a dual beam FEI Novalab 660 at The University of Manchester. The samples were then loaded into the Local Electrode Atom Probe (LEAP) Cameca - 3000X at The University of Oxford, and were held at a temperature of 50 K during data acquisition. The field evaporation of ions was carried out in laser pulse mode with a green laser of energy 0.4 nJ and a frequency of 200 kHz. The reconstruction of the analysed volumes was made on the basis of the needle profile from the SEM images of the sharpened needles.

For TEM analysis, electropolished foils were prepared for examination by grinding from the non-irradiated face to a thickness of ~160 μm and then electropolishing using a twin-jet Tenupol-5 electropolisher together with a Julabo FP50 cooling unit. An electrolyte of 10% perchloric acid and 20% 2-butoxyethanol in ethanol [13] was used to electropolish ~12-15 μm from both the irradiated and non-irradiated faces, the depth measured with a Keyence X200K 3D laser microscope. Subsequently, Elektron Technology's acid-resistant Lacomit varnish was used to protect the irradiated face while electropolishing to perforation from the non-irradiated face. The non-irradiated bulk material was prepared by the same method. All microscopy presented here was performed on a G2 80-200 kV spherical aberration-corrected (single, probe) FEI Titan microscope operating at 200 kV in scanning mode with a current of 0.6 nA. The microscope is equipped with a high brightness X-FEG source and the FEI ChemiSTEM™ system, comprising four energy-dispersive X-ray (EDX) detectors in close proximity to the sample, resulting in a total collection angle of 0.7 srad. While the sample was loaded in a low-background double-tilt holder, the determination of chemistry may be

considered to be semi-quantitative as the Cliff-Lorimer approach was used with calculated K-factors, assuming no absorption and not accounting for Fe-scattering from the pole piece. All chemical data was obtained by spectral imaging (a full spectrum up to 20 keV at every pixel), after which chemical maps were extracted for the relevant alloying elements. Foil thickness measurements were made by an assessment of intensity oscillations in convergent beam electron diffraction (CBED) patterns by way of the graphical method [35]. Error in thickness measurements are therefore assumed to be ±10%, given that great care was taken to obtain CBED patterns from the exact Bragg condition.

In the APT needle reconstruction we determined the dimensions of the rod-like features as follows. The rod-matrix interface was assumed to be the position at which the Fe concentration is equal to that of the average between rod-maximum and the matrix. For this calculation, 1D concentration profiles were generated across length and width dimensions of the rods with cylindrical regions of interest (ROIs) of dimensions defined by a length exceeding that of the rod and a constant diameter of 3nm. The 1D concentration profiles were consistently binned with 500 ions per sample and 200 ions per step. The composition of the rods was calculated with the volume ROI defined as a cylinder with a constant diameter of 2 nm and a reduced length to avoid the edge of the rod where the concentration is skewed and the Zr content becomes high due to the matrix contribution. This procedure limits edge effects when calculating concentrations. The detection of Ni was not carried out due to the overlapping of Ni^+ peaks with Sn^{2+} peaks at 58 and 60Da and the Ni^{2+} peak with Zr^{3+} peak at 30Da, leaving only 29Da for detection of Ni, proving difficult with the low concentration of Ni (Da = mass to charge ratio). The detection of Sn in the reconstruction was also erroneous due to the Sn ions

diffusing readily on the sample surface and evaporating towards the crystallographic poles of the Zr matrix [29].

To obtain the dimensions of the rod-like features by STEM, spectral imaging and the resulting Fe maps from the ⟨0001⟩ direction provided good contrast against the defective α-Zr matrix and was used to obtain detailed rod width information. BF STEM imaging from the ⟨11$\bar{2}$0⟩ matrix orientation gave the best contrast for rod length as opposed to the Fe or Cr EDX signal, which is weak from this orientation, in which the rods are side-on and at their thinnest in the transmission direction. For quantification of number density, four images were obtained in BF STEM from the ⟨0001⟩ matrix orientation of a single grain. The determination of matrix orientation was performed by indexing the Fast Fourier Transform (FFT) of a high resolution STEM image

The matrix orientation of a single needle was determined prior to APT by electron diffraction in a FEI Tecnai F30 FEG-TEM at the University of Manchester by use of the ASTAR automated crystal orientation mapping system [36], coupled with precession [37] at 0.8° at a rate of 100 Hz using the NanoMegas precession system to reduce dynamical effects. Precession typically increases the number of spots and improves the reliability of solutions [38] when indexed by comparison to simulated kinematical diffraction patterns in the ASTAR Index software V1.4. A probe diameter of ~3 nm was formed in TEM mode by using a 20 μm diameter condenser C2 aperture and a small spot size, resulting in a low beam current of ~26 pA. The diffraction patterns were recorded as a function of position and indexed according to phase and orientation.

4 RESULTS

The defect structures after proton irradiation to nominally 2.3 dpa involve two distinct defect types that can be observed from or close to the $\langle 11\bar{2}0 \rangle$ matrix orientation. Figure 2 shows BF-STEM micrographs of the defect types, both of which have some degree of alignment in the (0001) basal plane. Neither type of defect was observed in non-irradiated material. Type I defects are elliptical loops with their long axis (10-20 nm) parallel to the $\langle 0001 \rangle$ direction and their short axis (5-10 nm) in the (0001) plane. Type II defects are linear defects with a short width 2-3 nm (Figure 2a and b), are of relatively sharp contrast and, from this $\langle 11\bar{2}0 \rangle$ matrix orientation, either have their long axis parallel to the $\langle 0001 \rangle$ direction or inclined to it by an angle between 12° and 15° (Figure 2b). Type II defects are distinct from the Type I in that they are visible when imaged parallel to the **g** = 0002 systematic row (Figure 2b), which the dislocation loops are not. This implies that the Type I defects are dislocation loops with a purely $\langle a \rangle$-component Burger's vector and these are assessed in detail elsewhere [15]. The nature of the Type II defects will be the focus of the remainder of this work.

From the analysis of four representative BF STEM images from the $\langle 11\bar{2}0 \rangle$ matrix orientation, it is estimated that ~30% of the Type II defects have their long axis parallel to $\langle 0001 \rangle$ and ~70% are inclined to the $\langle 0001 \rangle$ axis. However, when imaged from the $\langle 10\bar{1}0 \rangle$ orientation all Type II defects seem parallel to the $\langle 0001 \rangle$. Further, in BF STEM it was observed those of shorter lengths (< ~20 nm) have their length parallel to $\langle 0001 \rangle$ whereas those with longer lengths tended to be inclined to $\langle 0001 \rangle$. Therefore it is likely the case that all rods are tilted with respect to $\langle 0001 \rangle$ and the shorter, parallel rods are tilted in a symmetric orientation but appear parallel due to issues of projection. Figure

2c and d, demonstrate that Type II defects may be imaged end-on from the $\langle 0001 \rangle$ direction. The defects highlighted in Figure 2c and d are projected as circles or ellipses, suggesting that the Type II defects are rods and not platelets. Therefore, due to their morphology, the Type II defects will be referred to as rods hereafter. From the $\langle 0001 \rangle$ orientation, the number density of rods was calculated as 7.01 ±0.77 x10^{21} m^{-3}, with the error given being a single standard deviation from the mean number of defects counted between four different images within the same grain, resulting in a count of 422 defects. If we assume that rods are observed edge-on from the $\langle 11\bar{2}0 \rangle$ orientation, a defect tilted 12° from $\langle 0001 \rangle$ will have its long axis in the $\langle 1\bar{1}05 \rangle$ direction and a defect tilted 15° in the $\langle 1\bar{1}04 \rangle$.

A chemical analysis by STEM energy-dispersive X-ray spectroscopy (EDX) is given in Figure 3, demonstrating chemical segregation to the defects displayed in Figure 2b and Figure 2d. Comparing Figure 3a-c from the $\langle 11\bar{2}0 \rangle$ orientation with Figure 3d-f from the $\langle 0001 \rangle$ orientation immediately demonstrates the rod morphology. However, some rods are circular in cross section (Figure 3d bottom right) and some appear elliptical in cross section (Figure 3d top left and bottom left). Of the 33 rods studied by EDX from the $\langle 0001 \rangle$ orientation, 19 were circular and 14 elliptical. Of the 14 elliptical, 12 were elongated along the $\langle 1\bar{1}00 \rangle$ direction, consistent with the rod long axis in either the $\langle 1\bar{1}04 \rangle$ or $\langle 1\bar{1}05 \rangle$, 2 anomalies along $\langle 11\bar{2}0 \rangle$ and zero along any direction in between. All rods observed from the $\langle 0001 \rangle$ orientation were rich in Fe and Cr but not Ni. From the $\langle 11\bar{2}0 \rangle$ orientation, some Ni segregation was observed (Figure 3c), but this was uncommon.

The rod-like morphology of the precipitates was investigated by atom probe tomography (APT), an example of which is shown in Figure 4, where Fe and Cr enriched regions are shown by iso-concentration surfaces for the volumes with Fe+Cr > 1.2 at%. Figure 4a is rotated around the long tip axis by 90° to produce Figure 4b in order to demonstrate their common direction. A total of 5 APT needles were analysed from non-irradiated Zircaloy-2 and a total of 7 needles for the proton-irradiated Zircaloy-2. Of the 5 non-irradiated needles analysed, no rods were observed. All 7 irradiated APT needles analysed contained rods with their long axis in a common direction, such as those in Figure 4. All rods were enriched with both Fe and Cr.

To assess whether the rods that we observe in APT are the same as those that we observe in the TEM, we conducted a study to determine the common orientation of the rods in the APT tips by performing both TEM diffraction analysis and APT on the same tip. In Figure 5a and b we show the precession selected area diffraction patterns (pSADPs) from TEM with BF-TEM image inserts. In Figure 5c and d we show the automatic indexing of those patterns on the stereographic triangle and in Figure 5e we plot these orientations on a Kikuchi map. Figure 5f displays the APT Fe data for that same tip, in which two rods were found at an angle ~20° to the tip axis. In Figure 5a the tip is rotated about the tip axis by 8° relative to that in Figure 5b. In Figure 5c and d the precession selected area diffraction patterns are indexed as the $\langle \overline{15}\, 3\, 12\, \overline{6} \rangle$ and the $\langle \overline{11}\, 1\, 10\, \overline{3} \rangle$ for the diffraction patterns in Figure 5a and b, respectively. The angle between two vectors in a hcp system may be calculated after Frank [39], and, as a sanity check, the angle between these two indexed orientations is 7.6°. The cross product of two vectors gives their mutual perpendicular vector. The Miller-Bravais indices were converted to Miller indices, the cross product obtained and then converted back to

Miller-Bravais to give the tip axis orientation $\langle 11\,\overline{13}\,2\,\overline{18}\rangle$. The angle between this vector and the unique $\langle 0001 \rangle$ direction is 36.1°. The Kikuchi map in Figure 5d demonstrates a way in which we can check that this is correct; the common plane that connects the two orientations (dotted in orange) is the plane of the tip cross section and the angle of this plane with the $(1\overline{2}10)$ plane gives the angle of the tip cross-section with the $\langle 0001 \rangle$ orientation; 54.4°. The tip axis is therefore 90-54.4 = 35.6° from the $\langle 0001 \rangle$ orientation, a value that is very similar to the 36.1° obtained from the cross product method. While we do not know the rotation of the APT tip around its axis with respect to the orientation at which the diffraction data was collected, the rods in Figure 4c are ~20° from the tip axis and therefore, at a minimum, their long axis is 36-20 = 16° from the $\langle 0001 \rangle$ Zr matrix orientation, which is consistent with the 12-15° inclination measured by TEM from the $\langle 11\overline{2}0 \rangle$ matrix orientation, Figure 2.

The distribution in rod diameter and length has been determined by both APT and STEM techniques. The data are displayed as number frequency histograms in Figure 6, which show good agreement between the two techniques considering the small sample size. The reader is reminded that the two techniques correspond to slightly different dose levels of 1.5 and 2.3 dpa for APT (red) and BF STEM (grey), respectively. APT dimension measurements have shown no correlation between rod diameter and length. The rod diameter (Figure 6a) ranges 2-5 nm with the modal diameter at 3 nm. Both the APT and BF STEM data give rod lengths in the range ~5-30 nm, with APT more suitable for detecting rods in the lower end of this range. The APT lengths are slightly skewed towards a modal value of 12 nm, whereas the BF STEM data gives a wider range of 15-20 nm.

Chemical analysis of the rods has been performed by both STEM-EDX and APT. For STEM-EDX, the α-Zr matrix was orientated in the ⟨0001⟩ direction to observe the rods in their most concentrated form in the transmission direction and hence minimising Zr signal from the matrix. However, the matrix contribution remains large and so the atomic per cent (at.%) of Fe and Cr within the rods remain low at < 4 at.%. The Fe/Cr ratio is thought of as reliable due to the low solubility of the light transition elements in the α-Zr matrix [2–4]. The variation between 33 different rod compositions is displayed in Figure 7, where chemical data is plotted against rod diameter. The compositions are quantified in at.% Fe and Cr even though there is a large contribution from the Zr matrix and pole piece scattering effects are not taken into account. The data show that rods of ~3nm in diameter have higher Fe concentrations, which may suggest that these are the longest in the ⟨0001⟩ transmission direction and hence are most stable when 3 nm in diameter. While this is supported by the modal diameter of rods as 3 nm (Figure 6a), APT measurements have shown no correlation between diameter and length. As the thickness of the TEM foil in the ⟨0001⟩ direction is known and the mean rod length determined from the ⟨11$\bar{2}$0⟩ orientation is also known (~17 nm), we may estimate the stoichiometry of the rods at $Zr_3(Fe_{0.7},Cr_{0.3})$, although the Zr contribution is difficult to be certain of.

Figure 8a shows the distribution in the Fe/Cr atomic ratio as determined by both APT (red) and by STEM-EDX from the ⟨0001⟩ matrix orientation (grey patterned, averaged over the entire rod), which are directly comparable under the assumption that the concentration of Fe and Cr in the matrix is 0 at.% and so do not affect the STEM-EDX results. There is some agreement in the modal value between the two techniques, but APT gives a smaller range at Fe/Cr ~1-2.5 with a modal value of 2 compared to Fe/Cr

~1-6.5 and STEM-EDX gives a modal value of 2-3. Figure 8b shows the distribution of the APT-determined atomic ratios Zr/(Fe+Cr) (grey open circles) and Fe/Cr (red closed circles). This demonstrates that larger rods > ~400 nm^3 have lower Zr content. Considering both Figure 8a and b, it may be concluded that the average rod Fe/Cr = 2 and Zr/(Fe+Cr) = 4. As such, the mean composition of the rods as determined by APT at ~1.5 dpa is $Zr_4(Fe_{0.67}Cr_{0.33})$, tending towards $Zr_{3.1}(Fe_{0.67}Cr_{0.33})$ for rods of volume > ~400 nm^3. Also included in Figure 8b are the compositions of two Zr-Fe-Cr second phase particles (SPPs, size unknown due to intersection with needle edge) observed by APT in non-irradiated Zircaloy-2 with compositions $Zr_{1.2}(Fe_{0.47}Cr_{0.53})_2$ and $Zr_{1.1}(Fe_{0.49}Cr_{0.51})_2$. As such, the non-irradiated SPPs are of a significantly different composition compared to the irradiation-induced rod precipitates.

In using STEM-EDX, it is possible to consider the rod composition in relation to the closest second phase particle (SPP). A qualitative example is given in Figure 9, which shows chemical maps from the $\langle 1\bar{1}00 \rangle$ matrix orientation. At the $\langle 1\bar{1}00 \rangle$ matrix orientation the rods are inclined directly out of the plane of the image ($\langle 1\bar{1}04 \rangle$ or $\langle 1\bar{1}05 \rangle$), and, as such, all rods appear to have their long axis parallel to $\langle 0001 \rangle$. This highlights the importance of analysis from multiple orientations in the TEM, an issue avoided in APT. It is clear from Figure 9 that the rods align with one another in the basal plane. While this was a common observation in the TEM samples, the APT samples revealed no such alignment. In Figure 9, the rods with the highest BF contrast and the greatest EDX signal arising from Fe+Cr are the rods that are closest to the dissolving SPP; those at the top of figure are relatively weak in contrast.

The chemical composition of the 33 rods quantified by STEM-EDX from the matrix ⟨0001⟩ orientation in Figure 6a and Figure 7 were binned into 50 nm wide annular segments from the nearest Fe-Cr type pre-existing SPP. The results are displayed in Figure 10, where data points are the average rod composition in that radial distance bin, i.e. in bins of 50 nm up to a maximum distance of 300 nm. Note that foil thickness is assumed to vary little within this region. While the errors from single standard deviations are significant, it can be seen that both the Fe and Cr content of rods decrease with increasing distance from the closest Fe-Cr SPP. It can also be seen that the Cr concentration decreases more rapidly than Fe with respect to radial distance after a radius 200 nm, causing the Fe/Cr atomic ratio to increase sharply at this distance.

Matrix compositions were calculated from APT data in both irradiated and non-irradiated samples with Region of Interest (ROI) volumes containing no segregations or clusters of atoms. For this calculation, ~20 million ions were used in the non-irradiated ~30 million ions in the proton-irradiated case. The matrix has 0.023 at% Fe and 0.020 at% Cr in the non-irradiated condition, while after irradiation the concentration increases to 0.053 at% Fe and 0.034 at% Cr, with a relative standard deviation of ~50%.

5   DISCUSSION

We have characterised rod-shaped structures in Zircaloy-2 plate after proton irradiation by both atom probe tomography (APT) and scanning transmission electron microscopy (STEM) coupled with energy-dispersive X-ray (EDX) spectroscopy. In the APT data all rods within a single α-Zr grain were orientated in the same manner, as exemplified in the 90° rotation around the needle axis between Figure 4a and b. While

the uniqueness of the rod orientation may suggest that the rod long axis is in the $\langle 0001 \rangle$ direction, BF-STEM and STEM-EDX from the $\langle 11\bar{2}0 \rangle$ and $\langle 10\bar{1}0 \rangle$ matrix zone axis, Figure 2 and Figure 9, suggest that the rods are inclined to $\langle 0001 \rangle$ by $\sim\pm12\text{-}15°$. This is confirmed by correlating TEM diffraction data and APT data from the same tip, Figure 5. In Figure 3c we show an inclined rod rich in Ni. Whilst this has been suggested previously [25], we did not observe this frequently due to a delay in Fe-Ni type SPP dissolution relative to the Fe-Cr type SPP at this irradiation dose level [40].

Previously reported rod-shaped irradiation-induced precipitates have been observed after neutron irradiations at high fluxes, high temperatures and/or to high fluences [17,24]. Under normal power reactor conditions they have only been observed after post-irradiation annealing, resulting in the growth of such features [17]. These rods have been shown to have their long axis in $\langle 0001 \rangle$ and to align in basal planes. Power reactor fluxes result in a dose rate of $\sim 1 \times 10^{-7}$ dpa s^{-1} [41,42] at ~ 310 °C [43], and, as such, the proton irradiations here provide both a high damage rate and irradiation temperature, which seem to be necessary requirements for the nucleation of these features. It should be noted that no Sn-rich precipitates have been observed in the present work. The precipitation of Zr_5Sn_3 has been observed after neutron irradiation at high flux and temperature and has been attributed to irradiation-enhanced diffusion [17,24].

The rod dimensions demonstrated in the present work show good agreement in measurements made between APT and BF STEM or STEM-EDX mapping, Figure 6, although the APT measurements may be skewed towards rods of shorter length due to the small analysed volume and the ignoring of larger rods that cut the APT needle

surface. In regards to rod composition, it should be noted that larger scatter in measurements is expected from smaller rods as less ions are used in the calculation. While there does not seem to be much variation in rod composition with respect to rod volume, as determined by APT, Figure 8b, there may be a tendency away from $Zr_4(Fe,Cr)$ and towards $Zr_3(Fe,Cr)$ after rod volumes exceed 400 nm^3 (Fe/Cr ~2 in both cases). As rods in the TEM samples may be longer than that of the APT samples, the stoichiometry estimated from STEM-EDX as $Zr_3(Fe,Cr)$ (Fe/Cr ~2) may suggest that rods do indeed start with an atomic ratio Zr/(Fe+Cr) ~4 that tends to ~3 as the rods increase in size as second phase particles continue to dissolve and disperse solute into the matrix [6,16,17]. The Fe/Cr ratio has been shown to increase at distances > ~ 200 nm from the closest partially-dissolved $Zr(Fe,Cr)_2$ SPP, Figure 10, which is an indication that the rods nucleate as a result of irradiation-induced dissolute and solute redistribution, in addition to having a dependence on the relative diffusivities of Fe and Cr in the α-Zr matrix, Fe > Cr [44]. Of course, due to the issue of projection in the transmission direction, there is uncertainty in that we cannot determine the distance of a rod from the SPP in the direction normal to the surface of the TEM foil. However, it is the case that rods rich in Fe and Cr are more frequently found close to partially-dissolved $Zr(Fe,Cr)_2$ SPPs in neutron-irradiated material [25].

While the existence of the $Zr_4(Fe,Cr)$ phase has been deemed 'questionable' by some [45], as it is not present in the Zr-Fe binary phase diagram [46,47], it has been reported in material after quenching from the α+β- or β-phase region, and is known to dissolve quickly at low fluences [6,48]. As such, it is thought to be a metastable phase and may be instrumental in the nucleation of the rods presented here. The Zr_3Fe phase, alternatively, has been reported in the literature to nucleate in Zircaloy-4-type alloys

under PWR conditions [26] and in Zircaloy-2 under BWR conditions [27]. Zr-Fe phases are found in the non-irradiated state if the Fe/Cr > 4 (wt.%) in the total alloy composition [3], resulting in the nucleation of either Zr_3Fe or Zr_2Fe, the preference for which has been suggested depends on cooling rates [3]. The Zr_3Fe phase has been shown as stable under neutron irradiation at ~315-350 °C in regards to both changes in chemistry and structure [26,28], although its amorphisation behaviour under electron irradiation is well known [49,50]. Such stability may be predicted if one considers the low melting point of the Zr_3Fe phase (885 °C) in comparison to other phases, e.g. $Zr(Fe,Cr)_2$ T_{melt} = 1630 °C [51]. As such, for a given irradiation temperature, the Zr_3Fe SPP might be better able to recover the damage incurred by thermal annealing effects in comparison to high T_{melt} SPPs. Further, the growth rate of Zr_3Fe SPPs has been shown as greater than that of $Zr(Fe,Cr)_2$ in non-irradiated material during heat treatments [26] and multiple epitaxial relationships between Zr_3Fe and the α-Zr matrix have been reported [45]. Barberis *et al.* argued that the almost isotropic nature of the interfacial energy must mean that is not a dominating factor influencing SPP nucleation and stabilisation [45]. If the rods investigated here are indeed Zr3Fe in structure, their morphology must be due to the preferential ⟨0001⟩ diffusional anisotropy of Fe, Cr and Ni in α-Zr [52], supported by their observation under high neutron irradiation temperatures and flux [17,24].

The rods observed in the present work are thought to be crystalline for the following reasons, namely the alignment of the rods with the crystallography of the α-Zr matrix and with one another, and the general consistency in chemical composition, both between different rods and within individual rods, the latter investigated by the use of proxigrams [53]. However, the rods proved too small for structural analysis by electron

diffraction. In the literature, Zr_3Fe is observed with orthorhombic crystal structure with lattice parameters a = 0.33 nm, b = 1.1 nm and c = 0.88 nm [3].

The geometric arrangement of clusters during the early stages of precipitation has been investigated recently by Burr *et al.* using *ab initio* DFT calculations, which show that clusters of Fe, Cr or Fe+Cr around a Zr vacancy induce less lattice strain than that of an isolated interstitial defect [30]. The proposed necessity of a Zr vacancy defect for Fe and Cr clustering is interesting, as it helps explain the correlation between matrix solute content and vacancy c-loop nucleation [12] and the existence of a high density of vacancy c-loops in the vicinity of partially-dissolved SPPs [13,12,14]. The growth of clusters may be attributed to their increasing stability with increasing size; recent calculations by Varvenne *et al.* have shown that the binding energy, and therefore the stability, of clusters increases with n up to $n = 7$ [54] where n refers to the number of atoms/vacancies in the cluster, with the most stable configurations as 3D clusters, in agreement with earlier calculations for clusters of $\leq$ 10 vacancies [55,56]. Larger vacancy clusters may induce the nucleation of larger Fe, Cr clusters [30].

In the present work we find rods and not clusters, but clusters that contain predominantly Fe and Cr (Ni to a much lesser extent) have recently been detected by APT in Zircaloy-2 cladding material after irradiation in a BWR to a high fluence of 16.5 $\times 10^{25}$ n m^{-2} ~27.5 dpa [29]. While the cluster composition was highly variable in the 1-5 nm diameter clusters, and, as such, the structure likely non-crystallographic, Sundell *et al.* clearly demonstrated that the clusters segregate in planar arrays separated by a distance of ~10 nm [29]. These planes were assumed to be basal (0001) planes due to their uniqueness, but orientation information was not available from the APT data sets.

The calculations by Burr *et al.* demonstrate clustering predominantly in basal planes [30], which agrees with the alignment between rods in the present work and corroborates the assumed plane in the work of Sundell *et al.* [29] and the alignment between irradiation-induced precipitates in the basal plane reported in the literature [17,24]. The number density of clusters reported by APT in neutron-irradiated material was high at $8 \pm 2 \times 10^{23}$ m^{-3}. The number density of a-loops is given by Carpenter and Northwood at 25 dpa (a slightly lower dose than that of Sundell et al.) as $\sim 2 \times 10^{22}$ m^{-3} [57], which indicates that the cluster number density is higher than that of a-loops by a factor of 40, although Sundell et al. suggest a factor of 10. In the present work, the density of rods is calculated to be $7.01 \pm 0.77 \times 10^{21}$ m^{-3}. According to Carpenter and Northwood, the a-loop number density at ~ 2.3 dpa should be close to 3×10^{22} m^{-3} for neutron irradiated Zircaloy-2 [57], which is higher than the rod density by a factor of ~ 4. However, the a-loop number density that we have calculated for the proton-irradiated Zircaloy-2 is lower at $2.14 \pm 0.73 \times 10^{21}$ m^{-3}[15], and, as such, the rod number density is higher than that of the a-loop number density by a factor of ~ 3. If one considers the volume of material exhibiting clustering behaviour by Sundell *et al.* (assuming an average cluster sphere of diameter 3 nm) and that of the present work, combining the APT and STEM measurements, the total volume fraction of clusters in the former ($\sim 1.1e^{-3}$) is higher than that presented here ($\sim 1.2e^{-4}$) by a factor of ~ 9. Such a difference may be related to the higher degree of SPP irradiation-induced dissolution at the higher dose studied by Sundell *et al*.

The high density of clusters and rods observed after irradiation is likely to have an effect on macroscopic properties. The alignment of rods in the (0001) plane presented here is similar to the alignment of a-loops in neutron-irradiated material [58] and so we

may expect significant interactions between the two structures. Chemical segregation to dislocation loops has been discussed as likely to change the loop bias for point defects and clusters, and, as such, is thought to be important in the stability, shape and evolution of dislocation structures [25]. The influence of solute on c-loop density is well known [12] and a high density of c-loops is correlated to the accelerated regime of irradiation-induced growth [59]. Further, the effect of variable solute segregation to dislocations in different alloys and at different irradiation doses has been suggested as a source of variation in both a-loop size and in irradiation-induced hardening measurements in Zircaloy-2 and -4 [22,31,32]. As dislocation loops are thought to be intrinsically related to macroscopic irradiation-induced growth strain, their interaction with dispersed solute and its clustering is worthy of further investigation.

6   CONCLUSIONS

We have investigated the nature of nano-rods that precipitate as a result of proton irradiation and have discussed their importance with regard to their neutron-irradiation analogues. We have utilised correlative analysis in APT, electron diffraction and STEM-EDX, with good agreement between the techniques in terms of rod morphology, crystallography, dimensions and composition. Small rods are observed to have composition $Zr_4(Fe_{0.67}Cr_{0.33})$, tending towards $Zr_3(Fe_{0.69}Cr_{0.31})$ as the rod volume increases to > ~400 nm^3, and most rods are considered to have their long axis inclined to $\langle 0001 \rangle$ by 12-15°, i.e. in the $\langle 1\bar{1}04 \rangle$ or $\langle 1\bar{1}05 \rangle$ Zr matrix direction, similar to those observed in neutron irradiated material. The rod Fe/Cr atomic ratio is shown to increase at distances > ~200 nm from the closest partially-dissolved $Zr(Fe,Cr)_2$ SPP, suggesting that the rods nucleate as a result of the irradiation-induced dissolution of

pre-existing intermetallic phases and that their chemical composition depends on the relative diffusivities of Fe and Cr in the α-Zr matrix. At 2.3dpa, the number density of rods is calculated to be higher than that of a-loops by a factor of ~3. As such, the implications for macroscopic strain-related phenomena, such as irradiation-induced growth and hardening, may be significant.

7   ACKNOWLEDGEMENTS

8   REFERENCES

[1]   L. Hallstadius, S. Johnson, E. Lahoda, Cladding for high performance fuel, Prog. Nucl. Energy. 57 (2012) 71–76. doi:10.1016/j.pnucene.2011.10.008.

[2]   M.M. Stupel, M. Bamberger, B.Z. WEiss, Determination of Fe solubility in αZr by Mössbauer spectroscopy, Scr. Metall. 19 (1985) 739–740.

[3]   D. Charquet, R. Hahn, E. Ortlieb, J. Gros, J. Wadier, Solubility limits and formation of intermetallic precipitates in ZrSnFeCr alloys, Zircon. Nucl. Ind. Eighth Int. Symp. (1988) 405–422.

[4]   H. Zou, G.M. Hood, H. Nakajima, J. a. Roy, R.J. Schultz, The solid solubility of Ni and Co in α-Zr: a secondary ion mass spectrometry study, J. Nucl. Mater. 223 (1995)

186–188. doi:10.1016/0022-3115(95)00023-2.

[5]   R. Kuwae, K. Sato, E. Higashinakagawa, J. Kawashima, S. Nakamura, Mechanism of Zircaloy nodular corrosion, J. Nucl. Mater. 119 (1983) 229–239.

[6]   W.J.S. Yang, R.P. Tucker, R.B. Adamson, Precipitates in Zircaloy: Identification and the Effects of Irradiation and Thermal Treatment, J. Nucl. Mater. 138 (1986) 185–195.

[7]   M. Griffiths, R.W. Gilbert, V. Fidleris, R.P. Tucker, R.B. Adamson, Neutron damage in zirconium alloys irradiated at 644 to 710 K, J. Nucl. Mater. 150 (1987) 159–168. doi:10.1016/0022-3115(87)90071-7.

[8]   H. Zou, G.M. Hood, J. a. Roy, R.H. Packwood, V. Weatherall, Solute distribution in annealed Zircaloy-2 and Zr-2.5Nb, J. Nucl. Mater. 208 (1994) 159–165. doi:10.1016/0022-3115(94)90207-0.

[9]   H. Okamoto, Sn-Zr (Tin-zirconium), J. Phase Equilibria Diffus. 31 (2010) 411–412. doi:10.1007/s11669-010-9734-4.

[10] F. Garzarolli, R. Schumann, E. Steinberg, Corrosion optimized Zircaloy for boiling water reactor (BWR) fuel elements, Zircon. Nucl. Ind. Tenth Int. Symp. ASTM STP 1245. (1994) 709–723.

[11] S. Valizadeh, G. Ledergerber, S. Abolhassan, D. Jädernäs, M. Dahlbäck, E. V. Mader, G. Zhou, J. Wright, L. Hallstadius, Effects of Secondary Phase Particle Dissolution on the In-Reactor Performance of BWR Cladding, J. ASTM Int. 8 (2014) 729–753. doi:10.1520/JAI103025.

[12] M. Griffiths, R.W. Gilbert, The Formation of c-component defects in zirconium alloys during neutron irradiation, J. Nucl. Mater. 150 (1987) 169–181.

[13] L. Tournadre, F. Onimus, J.-L. Béchade, D. Gilbon, J.-M. Cloué, J.-P. Mardon, X. Feaugas, O. Toader, C. Bachelet, Experimental study of the nucleation and growth of c-component loops under charged particle irradiations of recrystallized Zircaloy-4, J. Nucl. Mater. 425 (2012) 76–82. doi:10.1016/j.jnucmat.2011.11.061.

[14] Y. de Carlan, C. Regnard, M. Griffiths, D. Gilbon, C. Lemaignan, Influence of Iron in the Nucleation of <c> Component Dislocation Loops in Irradiated Zircaloy-4, Zircon. Nucl. Ind. Elev. Int. Symp. ASTM STP 1295. (1996) 638–653.

[15] A. Harte, D. Jädernäs, M. Topping, P. Frankel, C. Race, J. Romero, L. Hallstadius, E.C. Darby, M. Preuss, The effect of matrix chemistry on dislocation evolution in an irradiated Zr alloy, Acta Mater. Submitted (2017).

[16] R.W. Gilbert, M. Griffiths, G.J.C. Carpenter, Amorphous intermetallics in neutron irradiated Zircaloys after hIgh fluences, J. Nucl. Mater. 135 (1985) 265–268.

[17] M. Griffiths, R.W. Gilbert, G.J.C. Carpenter, Phase instability, decomposition and resdistribution of intermetallic precipitates in Zircaloy-2 and -4 during neutron irradiation, J. Nucl. Mater. 150 (1987) 53–66. doi:10.1159/000361068.

[18] W.J.S. Yang, Precipitate stability in neutron-irradiated Zircaloy-4, J. Nucl. Mater. 158 (1988) 71–80.

[19] M. Griffiths, Comments on precipitate stability in neutron-irradiated Zircaloy-4, J. Nucl. Mater. 170 (1990) 294–300.

[20] X. Meng, D. Northwood, Second phases in Zircaloy-2, J. Nucl. Mater. 168 (1989)

125–136.

[21] Y. Etoh, S. Shimada, Neutron irradiation effects on intermetallic precipitates in Zircaloy as a function of fluence, J. Nucl. Mater. 200 (1993) 59–69. doi:10.1016/0022-3115(93)90009-N.

[22] B.V. Cockeram, K.J. Leonard, L.L. Snead, M.K. Miller, The use of a laser-assisted Local Electrode Atom Probe and TEM to examine the microstructure of Zircaloy and precipitate structure following low dose neutron irradiation at nominally 358°C, J. Nucl. Mater. 433 (2013) 460–478. doi:10.1016/j.jnucmat.2012.10.006.

[23] T. Sawabe, T. Sonoda, S. Kitajima, T. Kameyama, Analysis of atomic distribution in as-fabricated Zircaloy-2 claddings by atom probe tomography under high-energy pulsed laser, J. Nucl. Mater. 442 (2013) 168–174. doi:10.1016/j.jnucmat.2013.08.048.

[24] O.T. Woo, G.J.C. Carpenter, Radiation-induced precipitation in Zircaloy-2, J. Nucl. Mater. 159 (1988) 397–404.

[25] M. Griffiths, A review of microstructure evolution in zirconium alloys during irradiation, J. Nucl. Mater. 159 (1988) 190–218.

[26] F. Garzarolli, W. Goll, A. Seibold, I. Ray, Effect of In-PWR Irradiation on Size , Structure , and Composition of Intermetallic Precipitates of Zr Alloys, Zircon. Nucl. Ind. Elev. Int. Symp. ASTM STP 1295. (1996) 541–556.

[27] W. Goll, I. Ray, The Behavior of Intermetallic Precipitates in Highly Irradiated BWR LTP Cladding, Zircon. Nucl. Ind. Thirteen. Int. Symp. ASTM STP 1423. (2002) 80–95.

[28] V.N. Shishov, A. V Nikulina, V.A. Markelov, M.M. Peregud, A. V Kozlov, S.A. Averin, S.A. Kolbenkov, A.E. Novoselov, Influence of Neutron Irradiation on Dislocation Structure and Phase Composition of Zr-Base Alloys, Zircon. Nucl. Ind. Elev. Int. Symp. ASTM STP 1295. (1996) 603–622.

[29] G. Sundell, M. Thuvander, P. Tejland, M. Dahlback, L. Hallstadius, H.-O. Andren, Redistribution of alloying elements in Zircaloy-2 after in-reactor exposure, J. Nucl. Mater. 454 (2014) 178–185.

[30] P. a Burr, M.R. Wenman, B. Gault, M.P. Moody, M. Ivermark, M. Preuss, L. Edwards, R.W. Grimes, From solid solution to cluster formation of Fe and Cr in α-Zr, J. Nucl. Mater. 467 (2015) 320–331.

[31] B. V. Cockeram, K.J. Leonard, T.S. Byun, L.L. Snead, J.L. Hollenbeck, Development of microstructure and irradiation hardening of Zircaloy during low dose neutron irradiation at nominally 358 C, J. Nucl. Mater. 418 (2011) 46–61. doi:10.1016/j.jnucmat.2014.03.004.

[32] B. V. Cockeram, K.J. Leonard, T.S. Byun, L.L. Snead, J.L. Hollenbeck, Development of microstructure and irradiation hardening of Zircaloy during low dose neutron irradiation at nominally 377-440 C, J. Nucl. Mater. 449 (2014) 69–87. doi:10.1016/j.jnucmat.2014.03.004.

[33] R.E. Stoller, M.B. Toloczko, G.S. Was, A.G. Certain, S. Dwaraknath, F. a. Garner, On the use of SRIM for computing radiation damage exposure, Nucl. Instruments Methods Phys. Res. B. 310 (2013) 75–80. doi:10.1016/j.nimb.2013.05.008.

[34] G.S. Was, Fundamentals of Radiation Materials Science, in: Fundam. Radiat. Mater.

Sci., Springer Berlin Heidelberg New York, 2007: p. 83.

[35] D.B. Williams, C.B. Carter, 21.2 Thickness determination, in: Transm. Electron Microsc. A Textb. Mater. Sci., Springer Science+Business Media, LLC, 223 Spring Street, New York, NY, 10013, USA, 2009: pp. 352–354.

[36] E.F. Rauch, L. Dupy, Rapid spot diffraction patterns identification through template matching, Arch. Met. Mater. 50 (2005) 87–99.

[37] R. Vincent, P.A. Midgley, Double conical beam-rocking system for measurement of integrated electron diffraction intensities, Ultramicroscopy. 53 (1994) 271–282.

[38] E.F. Rauch, M. Véron, J. Portillo, D. Bultreys, Y. Maniette, S. Nicolopoulos, Automatic Crystal Orientation and Phase Mapping in TEM by Precession Diffraction, Microsc. Anal. 22 (2008) S5–S8.

[39] F.C. Frank, On miller–bravais indices and four-dimensional vectors, Acta Crystallogr. 18 (1965) 862–866. doi:10.1107/S0365110X65002116.

[40] A. Harte, M. Topping, P. Frankel, D. Jädernäs, J. Romero, L. Hallstadius, Nano-scale chemical evolution in a proton- and neutron-irradiated Zr alloy, J. Nucl. Mater. Submitt. (2016).

[41] V.N. Shishov, M.M. Peregud, A. V Nikulina, G.P. Kobylyansky, Z.E. Ostrovsky, Influence of structure-phase state of Nb containing Zr alloys on irradiation-induced growth, Zircon. Nucl. Ind. 14th Symp. 2 (2005) 666–685.

[42] R. Adamson, Charged particle bombardment of zirconium alloys: A review, Sweden, 2014.

[43] C.R.F. Azevedo, Selection of fuel cladding material for nuclear fission reactors, Eng. Fail. Anal. 18 (2011) 1943–1962. doi:10.1016/j.engfailanal.2011.06.010.

[44] R.A. Perez, H. Nakajima, F. Dyment, Diffusion in alpha-Ti and Zr, Mater. Trans. 44 (2003) 2–13.

[45] P. Barberis, N. Dupin, C. Lemaignan, A. Pasturel, J. Grange, Microstructure and Phase Control in Zr-Fe-Cr-Ni Alloys: Thermodynamic and Kinetic Aspects, J. ASTM Int. 2 (2005) 129–156. doi:10.1520/JAI12771.

[46] F. Stein, G. Sauthoff, M. Palm, Experimental determination of intermetallic phases, phase equilibria, and invariant reaction temperatures in the Fe-Zr system, J. Phase Equilibria. 23 (2002) 480–494. doi:10.1361/105497102770331172.

[47] H. Okamoto, Fe-Zr (iron-zirconium), J. Phase Equilibria Diffus. 27 (2006) 543–544. doi:10.1361/154770306X136601.

[48] B.-C. Cheng, R.M. Kruger, R.B. Adamson, Corrosion Behavior of Irradiated Zircaloy, Zircon. Nucl. Ind. Tenth Int. Symp. ASTM STP 1245. (1994).

[49] A.T. Motta, L.M. Howe, P.R. Okamoto, Amorphization kinetics of Zr3Fe under electron irradiation, J. Nucl. Mater. 205 (1993) 258–266.

[50] A.T. Motta, Amorphization of intermetallic compounds under irradiation — A review, J. Nucl. Mater. 244 (1997) 227–250. doi:10.1016/S0022-3115(96)00740-4.

[51] A.T. Motta, C. Lemaignan, A ballistic mixing model for the amorphization of precipitates in Zircaloy under neutron irradiation, J. Nucl. Mater. 195 (1992) 277–285. doi:10.1016/0022-3115(92)90519-Q.

[52] M. Christensen, W. Wolf, C.M. Freeman, E. Wimmer, R.B. Adamson, L. Hallstadius, P.E. Cantonwine, E.V. Mader, Effect of alloying elements on the properties of Zr and the Zr–H system, J. Nucl. Mater. 445 (2014) 241–250. doi:10.1016/j.jnucmat.2013.10.040.

[53] O.C. Hellman, J.A. Vandenbroucke, J. Rüsing, D. Isheim, D.N. Seidman, Analysis of Three-dimensional Atom-probe Data by the Proximity Histogram, Microsc. Microanal. 6 (2000) 437–444. doi:10.1007/s100050010051.

[54] C. Varvenne, O. Mackain, E. Clouet, Vacancy clustering in zirconium: An atomic-scale study, Acta Mater. 78 (2014) 65–77. doi:10.1016/j.actamat.2014.06.012.

[55] N. de Diego, A. Serra, D.J. Bacon, Y.N. Osetsky, On the structure and mobility of point defect clusters in alpha-zirconium: a comparison for two interatomic potential models, Model. Simul. Mater. Sci. Eng. 19 (2011) 35003.

[56] D. Kulikov, M. Hou, Vacancy dislocation loops in zirconium and their interaction with self-interstitial atoms, J. Nucl. Mater. 342 (2005) 131–140. doi:10.1016/j.jnucmat.2005.04.004.

[57] G.J.C. Carpenter, D.O. Northwood, The contribution of dislocation loops to radiation growth and creep of Zircaloy-2, J. Nucl. Mater. 56 (1975) 260–266.

[58] A. Jostsons, P.M. Kelly, G.R. Blake, The Nature of Dislocation Loops in Neutron Irradiated Zirconium, J. Nucl. Mater. 66 (1977) 236–256.

[59] R. a. Holt, R.W. Gilbert, c-component dislocations in annealed Zircaloy irradiated at about 570 K, J. Nucl. Mater. 137 (1986) 185–189. doi:10.1016/0022-3115(86)90218-7.
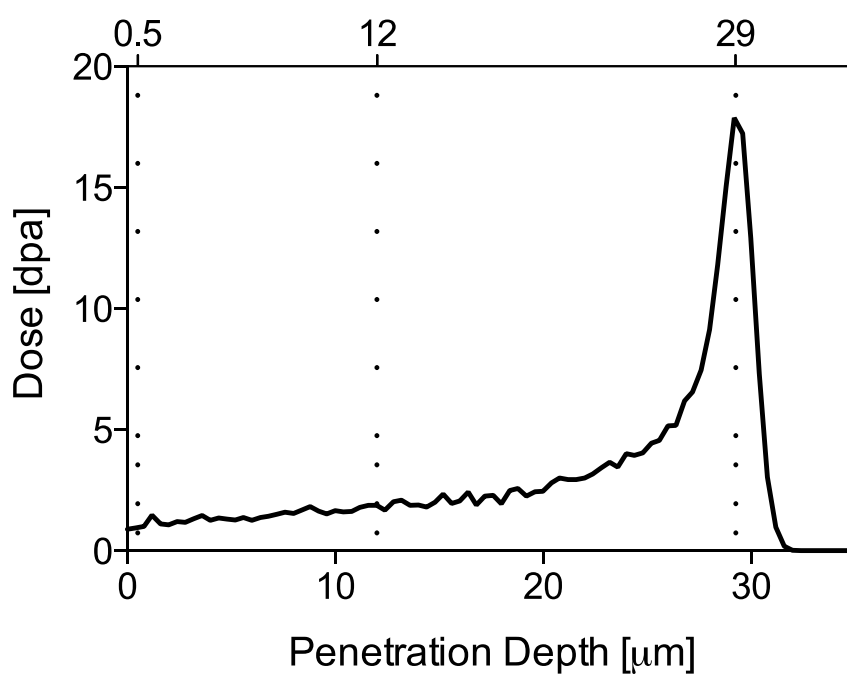
9 Figures

Figure 1 Damage profile in displacements per atom (dpa) for a pure, amorphous Zr matrix with the atomic density of pure, hcp α-Zr, calculated by SRIM with the quick Kinchin-Pease option (Ed(Zr) = 40 eV) and adjusted for 96 hr 2MeV proton irradiation at ~0.2 μA m^{-2}. The electropolished TEM foils were prepared at a depth of ~12 um (2.3 dpa), and the APT needles were prepared from the surface by FIB, resulting in a depth of ~0.5 um (1.5 dpa).
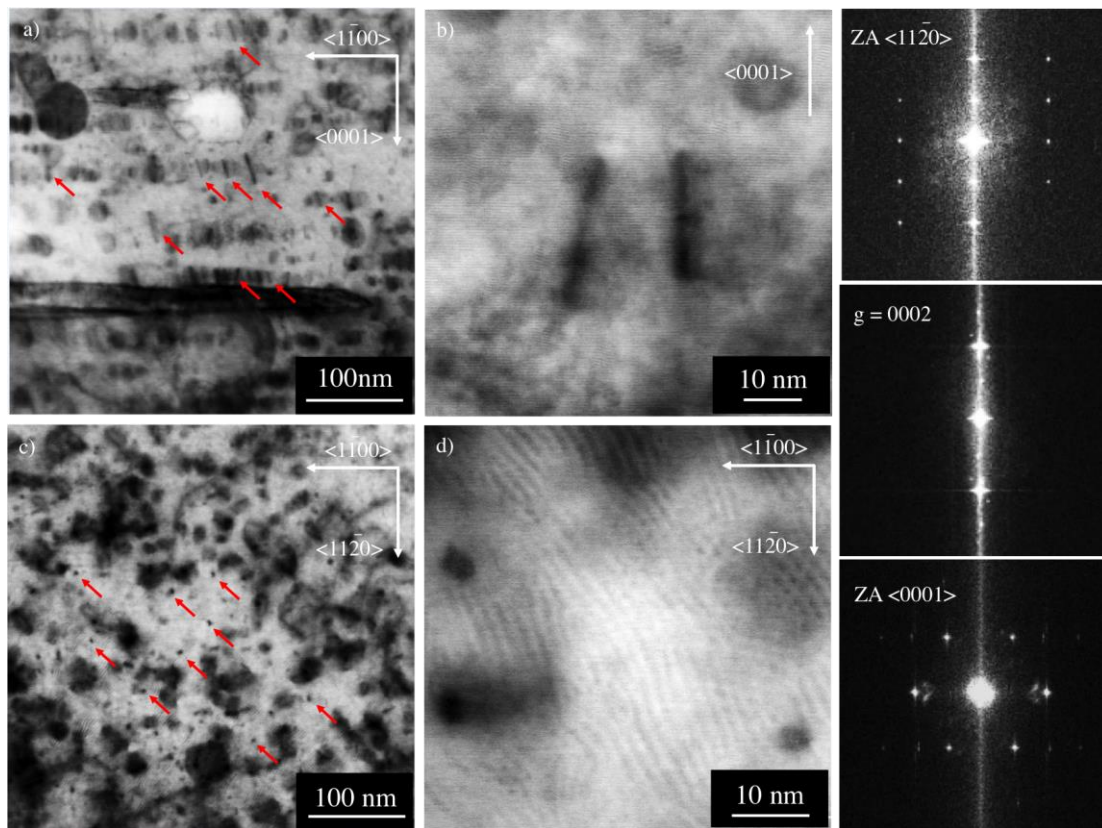
Figure 2 BF STEM micrographs from a) the $\langle 11\bar{2}0 \rangle$ zone axis, b) between the $\langle 11\bar{2}0 \rangle$ and $\langle 10\bar{1}0 \rangle$ zone axes parallel to the **g** = 0002 systematic row, and c) and d) from the $\langle 0001 \rangle$ zone axis. FFTs of HRSTEM images to the right give the relevant orientations. Rods are highlighted in a) and c) by red arrows.
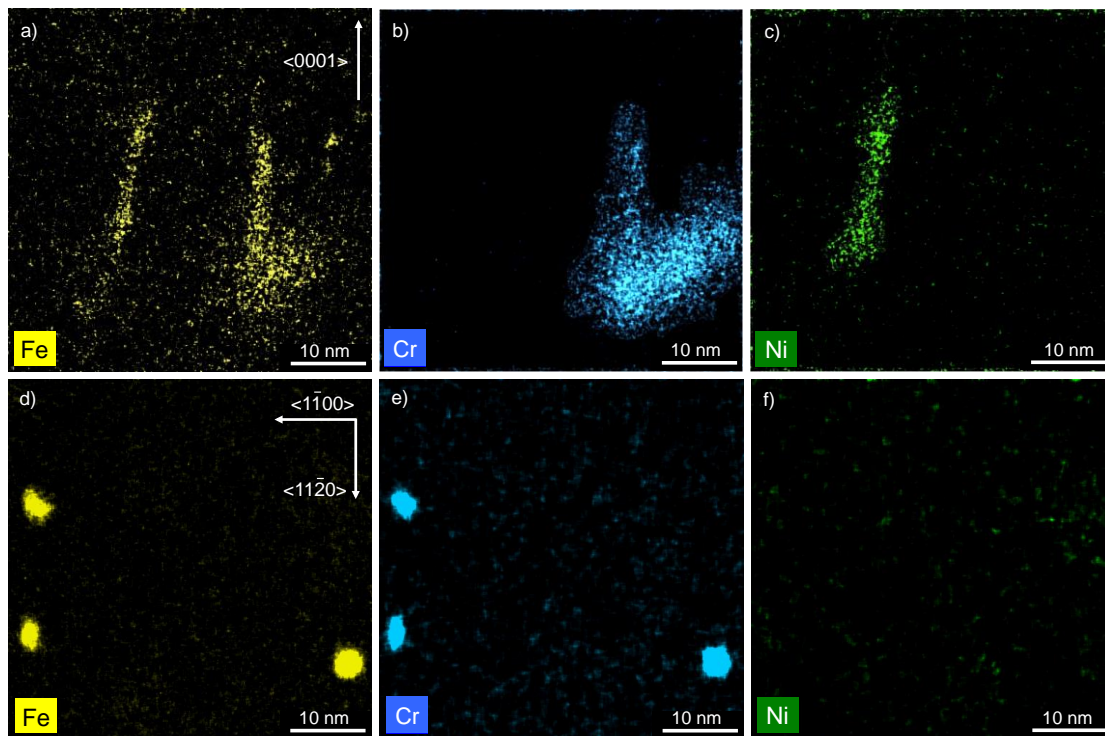
Figure 3 Qualitative chemical Fe, Cr and Ni maps by STEM-EDX from the a)-c) ⟨11$\bar{2}$0⟩ orientation relating to the BF STEM image in **Figure 2**b, and d)-f) from the ⟨**0001**⟩ orientation relating to **Figure 2**d.
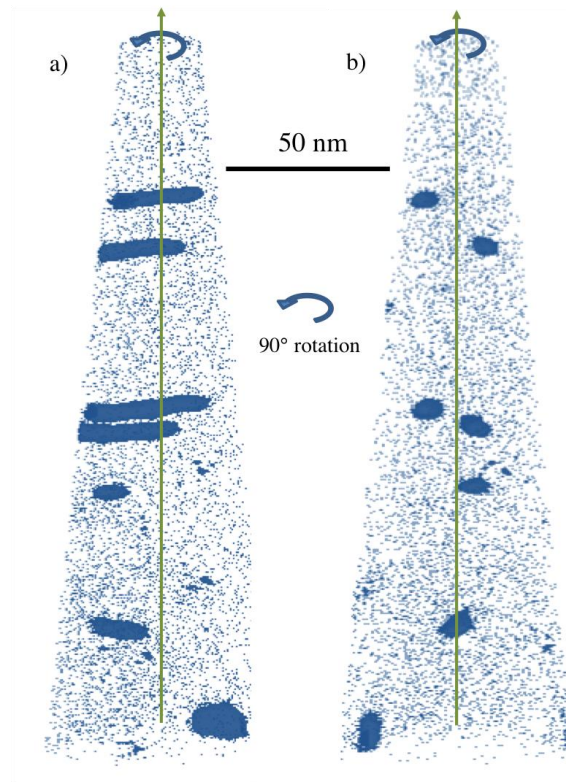
Figure 4 APT reconstruction showing the Fe+Cr iso-concentration surface (> 1.2 at%) rotated 90° to observe the irradiation-induced precipitates a) edge-on and b) end-on, demonstrating the rod-like morphology of the precipitates
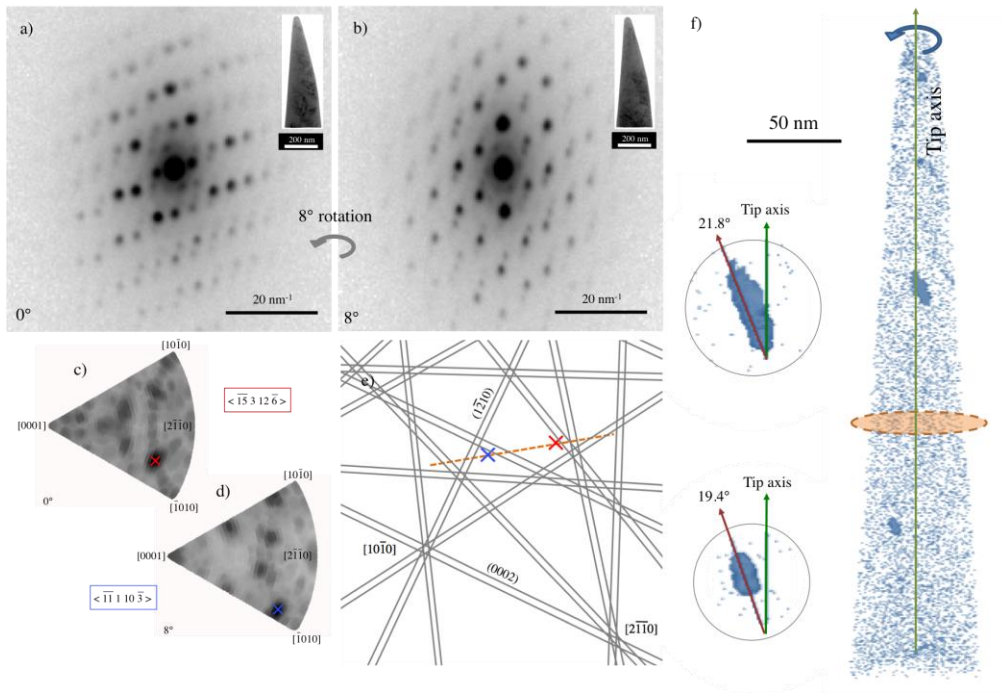
Figure 5 Determination of rod long axis direction with respect to the Zr matrix by correlative precession selected area diffraction (pSAD) and APT. Parts a) and b) show pSADPs at two rotations perpendicular to the tip axis. Parts c) and d) show the automatic indexing of those orientations on the stereographic triangle, and part e) on a Kikuchi map with their common plane dotted in orange. Part f) shows the same APT tip in Fe+Cr iso-concentration surface (> 1.2 at%) and the dotted orange cross sectional plane.
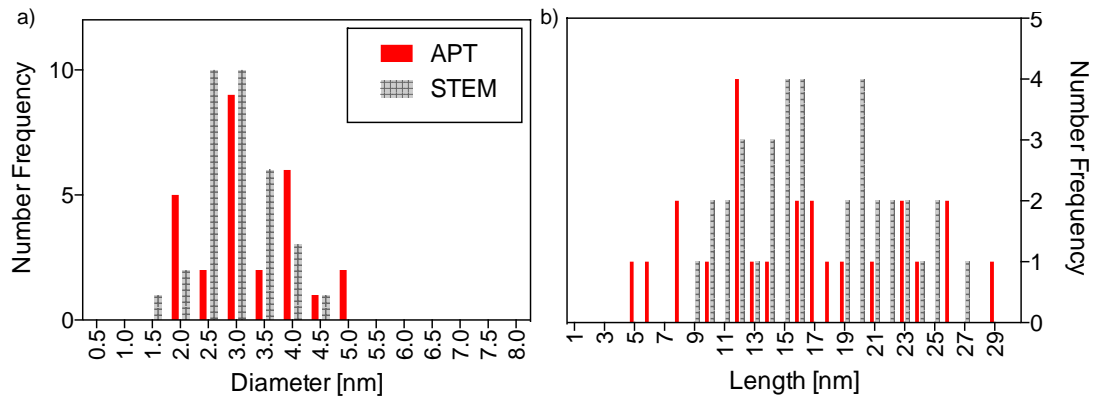
Figure 6 The distribution in rod a) diameter and b) length have been determined by APT (red) and BF STEM from the $\langle 11\bar{2}0 \rangle$ matrix orientation (grey patterned).
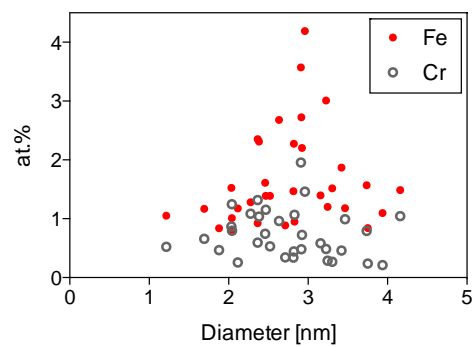

Figure 7 STEM-EDX determination of rod composition from the $\langle 0001 \rangle$ α-Zr orientation as a function of rod diameter.
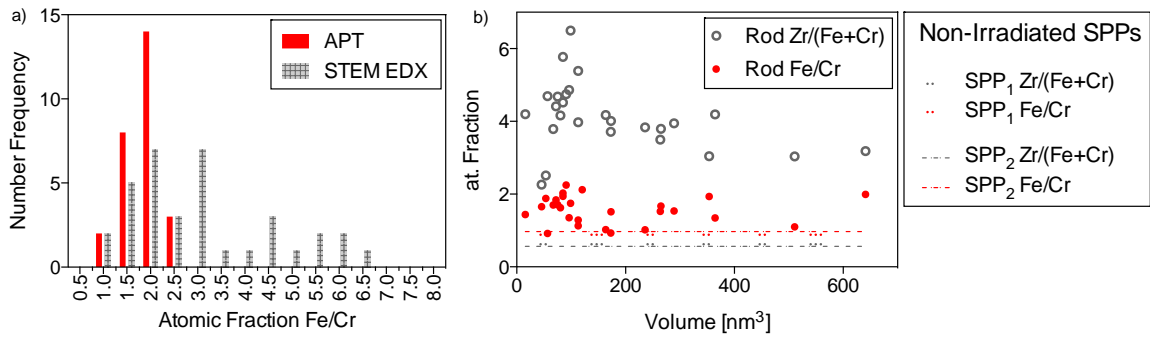
Figure 8 a) shows a rod Fe/Cr content frequency histogram as determined by APT (red) and STEM-EDX from the ⟨**0001**⟩ matrix orientation (grey patterned). Part b) is entirely derived from APT data and shows the Fe/Cr and the Zr/(Fe+Cr) atomic fractions of both the rods and two Zr-Fe-Cr SPPs.
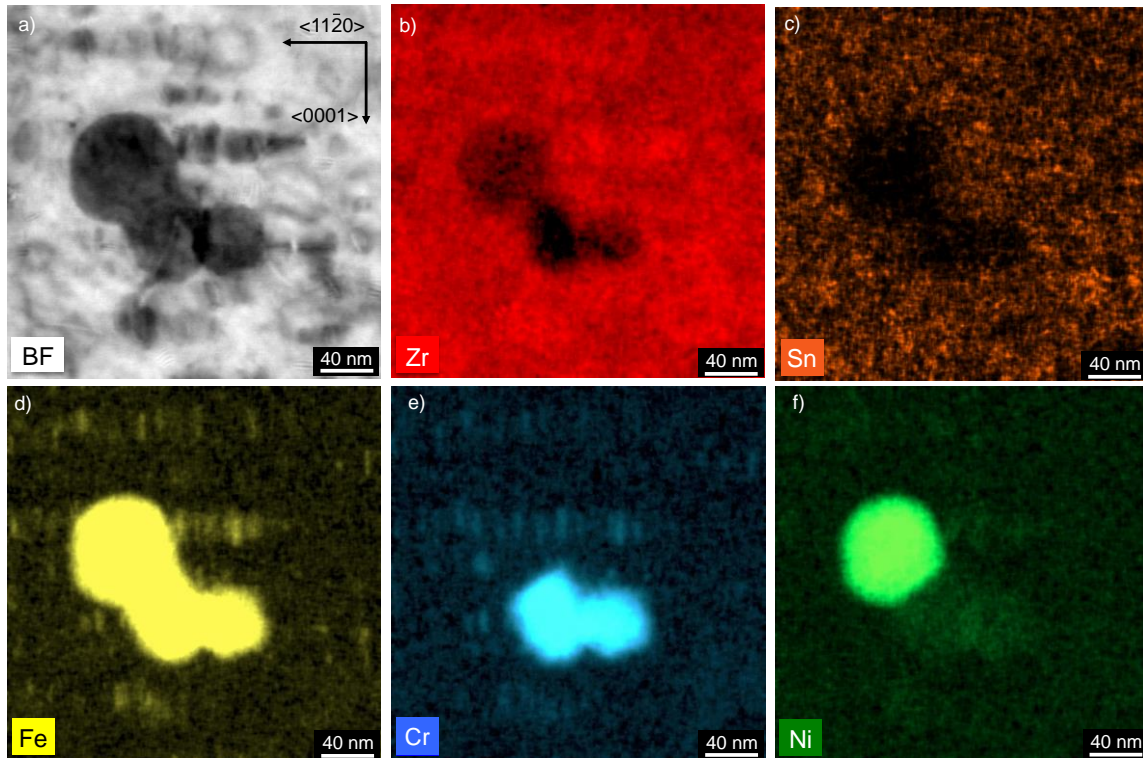
Figure 9 Irradiation-induced rods and their chemical components are shown in close proximity to pre-existing SPPs. The BF STEM image is given in a) and the chemical maps for Zr, Sn, Fe, Cr and Ni are shown in b)-f), respectively.
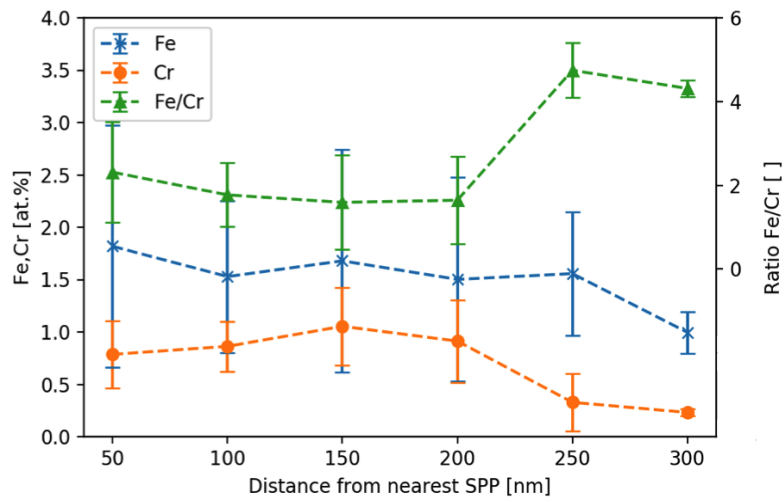
Figure 10 The composition of rods as a function of radial distance from the closest Fe-Cr SPP are shown. The whole data set comprises the 33 rods assessed in **Figure 6**a and **Figure 7**, and are binned into 50 nm increments in distance from an SPP. The errors bars are a single standard deviation from the mean.